



# Chemical bath deposited ZnO nanowires for H<sub>2</sub> gas sensing: Effect of deposition duration

Y. K. Abeykoon<sup>1,a)</sup>, A. A. I. Lakmal<sup>1</sup>, M. A. H. M. Munasinghe<sup>3</sup>, B. S. Dassanayake<sup>1,2</sup>,  
N. Gunawardhana<sup>3,a)</sup> 

<sup>1</sup>Postgraduate Institute of Science, University of Peradeniya, Peradeniya, Sri Lanka

<sup>2</sup>Department of Physics, Faculty of Science, University of Peradeniya, Peradeniya, Sri Lanka

<sup>3</sup>Office of Research and International Affairs, Sri Lanka Technological Campus, Padukka, Sri Lanka

<sup>a)</sup>Address all correspondence to these authors. e-mails: yashodaabeykoon84@gmail.com; nandag@sltc.ac.lk

Received: 1 May 2023; accepted: 9 November 2023; published online: 29 November 2023

This study explores the impact of deposition duration on the structural, morphological, and gas-sensing properties of ZnO nanowires (NWs). The ZnO NWs were chemical bath deposited on a spray-coated seed layer, which was deposited by the Jet Nebulizer Spray Pyrolysis method. The duration of chemical bath deposition varied from 2 to 8 h, and the deposited NWs were studied using XRD, SEM, and UV-visible spectroscopy. The experimental results indicate that all NWs had a hexagonal structure, with a diameter ranging from 75 to 155 nm and a length from 0.7 to 3  $\mu\text{m}$ . The gas sensing properties of the ZnO NWs were comprehensively evaluated with a focus on their response to H<sub>2</sub> gas using fabricated sensors at different operating temperatures. Consequently, it was revealed that the sensors show an optimum response of 9.36 for 100 ppm H<sub>2</sub> gas at 100 °C for the ZnO NWs grown for 6 h.

## Introduction

Hydrogen (H<sub>2</sub>) is a promising clean energy source due to its zero-carbon combustion. Industrial fields such as fuel cells, combustible engines, and catalysis [1, 2] commonly use H<sub>2</sub> for numerous purposes. Even though H<sub>2</sub> is a colourless, inflammable gas, it can cause explosions if the concentration of the gas exceeds 4% [2] (by volume) in the air due to the high burning velocity. H<sub>2</sub> is a strong reducing agent as well as a highly permeable gas. Therefore, in hydrogen-based industries, it is essential to detect H<sub>2</sub> leakages and measure the concentration of emissions rapidly and accurately. Hence, developing devices to detect such inflammable gases cheaply is crucial.

Conductometric gas sensors can detect trace amounts of H<sub>2</sub> gas and provide an electrical signal proportional to the H<sub>2</sub> concentration. Nowadays, H<sub>2</sub> gas sensors gain much attention over other conventional methods of H<sub>2</sub> detection, such as gas chromatographs, mass spectrometers, and specific ionisation gas pressure sensors due to their low cost, smaller size, and faster response [3].

ZnO is a frequently used material in gas sensors [4] since it possesses the ability to host many dopant elements such as Cu [5], Al [6], and Ag [7], as well as the possibility of fabricating

one-dimensional (1-D) nanostructures. 1-D nanostructures such as nanowires (NWs) [8], nanorods (NRs) [9], nanoribbons [10], and nanobelts (NBs) [11] are widely used in gas sensors due to their high surface-to-volume ratio.

ZnO has gained attention in sensor development due to its distinct electrical and optical characteristics, which are strongly related to its broad direct bandgap and high excitation binding energy. ZnO has a significantly large direct bandgap of about 3.37 eV compared to other semiconductors. This large bandgap gives rise to a high electron mobility, which is crucial for effective charge transport in semiconductor devices. In addition, ZnO has a high exciton binding energy, which is required to break an electron-hole pair in the material. ZnO is extremely sensitive to changes in the environment, such as the presence of gases or liquids, due to its high exciton binding energy. These molecules can alter the ZnO sensor's electronic and optical characteristics when they come into contact with it, which can lead to detectable changes in the sensor's output signal [12].

Gas phase and wet chemical methods are two key methods which are used to synthesize ZnO nanostructures. Gas phase methods include techniques such as pulsed laser deposition [13], aerosol-assisted chemical vapor deposition [14], and atomic layer deposition [15]. Unlike most wet chemical methods, most

gas phase techniques require complicated equipment and high-temperature conditions. Sol-gel electrophoretic deposition [16], microwave radiation-assisted solvothermal [17], hydrothermal [18], and chemical bath deposition (CBD) [19] are some of the wet chemical methods that can be employed in the fabrication of 1-D nanostructures. Out of these, CBD is more advantageous than the other methods, as it is a cost-effective process that requires low-temperature conditions and atmospheric pressure. Besides that, CBD can be used to grow nanostructures cheaply on substrates such as glass successfully. However, the CBD technique also has challenges such as potential waste disposal concerns associated with precursor solutions and lack of scalability

Seed layers can be used to fabricate vertically aligned nanostructures such as NRs, and NWs. A seed layer is a pre-treated substrate that provides nucleation sites to enhance the vertical alignment of nanostructures. The seed layer can be deposited using methods such as spin-coating [10], RF-sputtering [20], thermal deposition [21], and jet-nebulizer spray pyrolysis/spray-coating [22]. In literature, different pertinent factors such as seed layer (seed layer thickness and diameter of the seeds) [22–24], deposition time [25], and effective precursor concentrations such as  $Zn^{2+}$  and HMTA [25, 26] have been studied. For instance, Ji et al. have shown that the vertical alignment of the ZnO NWs tends to increase with the increment of seed layer thickness [23]. According to the study, the NW diameter increased from 50 to 130 nm when the seed layer thickness increased from 20 to 1000 nm. Raksha et al. successfully optimized the most suitable pH conditions for NW growth and thoroughly experimented with the characteristic changes by hosting dopant elements into ZnO NWs [27]. This research states that the optimum pH for doped and undoped ZnO NWs growth is 6.8 and 10.8, respectively. Furthermore, the role of HMTA and the effect of HMTA concentration, which affects the morphology of ZnO NWs synthesized via CBD, has been investigated by Parize et al. [25]. The evidence shows that HMTA reduces the radial growth of ZnO NWs by increasing the axial growth. Also, results state that HMTA directly affects the nucleation process of ZnO NWs.

In this reporting work, the effect of CBD deposition duration on the growth of ZnO NWs, in which the seed layer was deposited by the jet nebulizer spray pyrolysis technique, a rarely used technique to deposit seed layer, is investigated. The main scope of this study is to investigate the  $H_2$  gas sensing ability of NWs with respect to the deposition duration of CBD process.

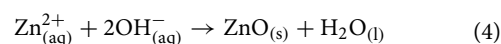
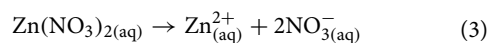
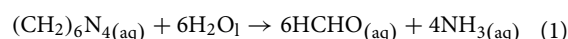
## Results and discussion

### Morphological characterization

The CBD process involves four consecutive stages: (a) incubation, (b) nucleation, (c) coalescence and (d) vertical growth. The CBD process is initialized with an incubation period.

The substrate is exposed to the precursor solutions,  $Zn(NO_3)_2 \cdot 6H_2O$  and hexamethylenetetramine/HMTA ( $C_6H_{12}N_4$ ), during this period. However, the rate of chemical reactions involved in this stage is extremely slow. Therefore, no evident growth can be seen. An observable growth can only be seen after the nucleation stage, where the rate of the chemical reaction is comparatively higher than in the previous stage. During the reaction, atomic, molecular or ionic species can be formed. These species tend to form secondary nucleation sites on the top of the nucleation sites of the ZnO seed layer. The coalescence stage involves the growth and merging of the nanoparticles on the secondary nucleation sites. This will form continuous NWs on the nucleation sites by accumulating the precursor molecules in the solution. At the final stage, subsequent vertical growth of NWs on the nucleation sites occurs by further accumulating the precursor molecules in the solution. This step will increase the length and the diameter of the NWs.

$Zn(NO_3)_2 \cdot 6H_2O$  and HMTA ( $CH_2)_6N_4$ ) undergo the following four consecutive reactions during the nucleation stage of ZnO nanowires directly on the glass substrate [25, 26]:



Additionally,  $Zn^{2+}$  and  $OH^-$  formed in Eq. 5 lead to the indirect crystallization of ZnO under specific conditions.

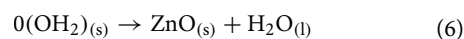
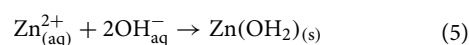
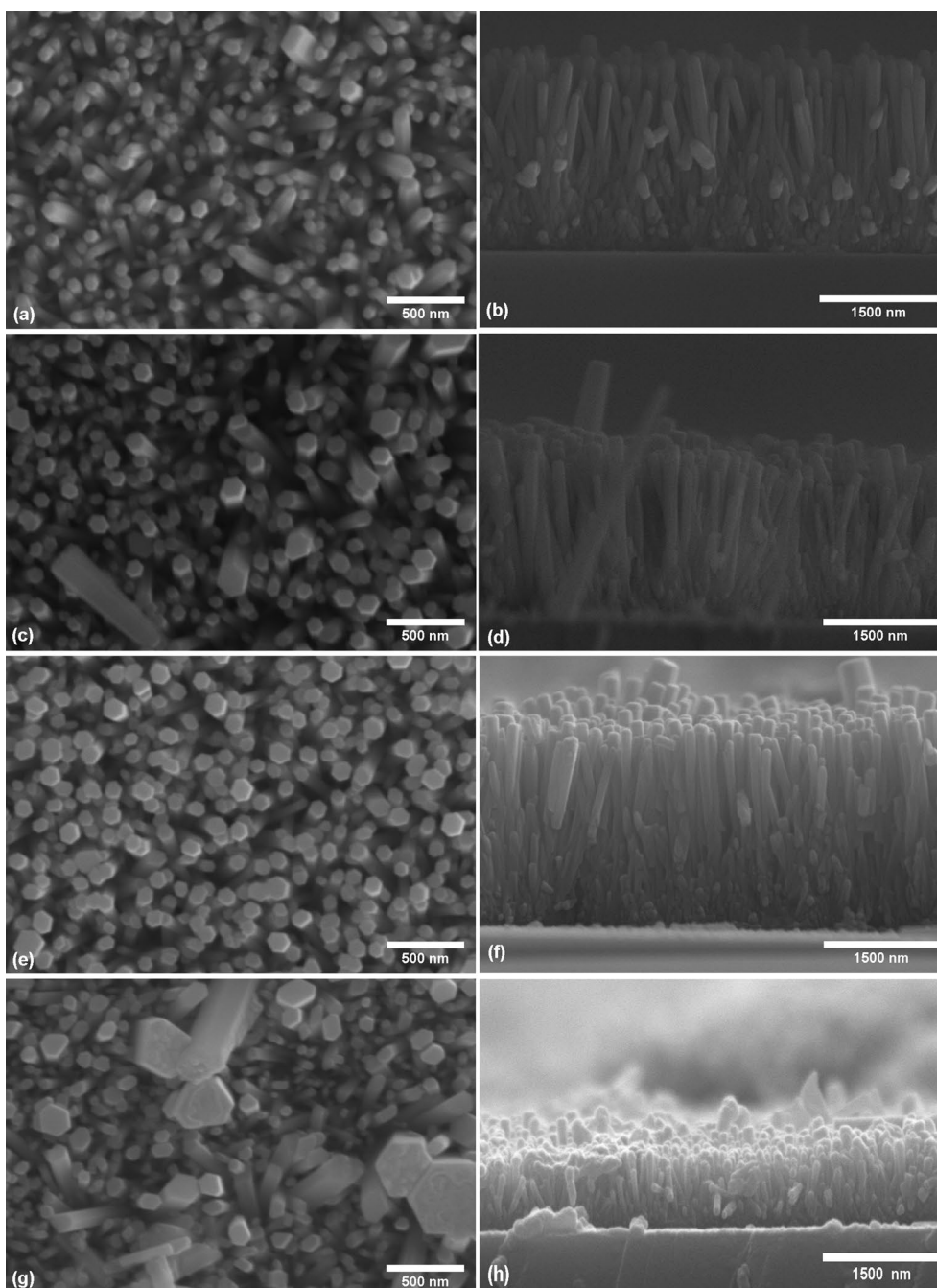


Figure 1 shows the SEM images of NWs grown on different CBD durations. The results reveal that with the increase of the deposition durations, the diameter/grain size of NWs increases, which is in agreement with the previous studies [24, 28]. As seen in Table 1, NWs grown for 8 h have the largest diameter. It can be seen that tiny NWs combine/coalesce with each other to form larger NWs. The length of the NWs increased up to 6 h from 2  $\mu m$  up to 3  $\mu m$ . However, when the deposition was increased up to 8 h, the length of the NWs was reduced to about 0.7  $\mu m$ .

The length of ZnO NWs typically decreases with increasing deposition duration due to a phenomenon known as self-termination or self-limitation. During the CBD process, the



**Figure 1:** The morphological and cross-sectional view of ZnO NWs grown at different deposition times: (a) and (b) 2 h, (c) and (d) 4 h, (e) and (f) 6 h and (g) and (h) 8 h.

**TABLE 1:** Morphological characteristics of ZnO nanowires deposited at different deposition times.

Deposition time (h)	NW diameter (nm)	NW length ( $\mu\text{m}$ )	Surface density	Aspect ratio
$2.00 \pm 0.01$	$65.0 \pm 0.5$	$1.80 \pm 0.07$	70	$25.0 \pm 0.5$
$4.00 \pm 0.01$	$90.0 \pm 0.9$	$2.20 \pm 0.03$	70	$27.0 \pm 0.9$
$6.00 \pm 0.01$	$97.0 \pm 0.8$	$2.90 \pm 0.01$	80	$35.0 \pm 0.8$
$8.00 \pm 0.01$	$125.0 \pm 0.8$	$0.70 \pm 0.01$	60	$5.0 \pm 0.8$

growth of NWs is driven by the chemical reaction between the precursor solution and the substrate. As the reaction proceeds, ZnO nuclei start to form on the surface of the substrate, which then grows into NWs. However, as the NWs grow longer, the concentration of the precursor solution near the tip of the NWs decreases due to the consumption of the precursor material by the growing NW. This decrease in precursor concentration near the NW tip can lead to a reduction of the growth rate of the NWs and eventually to the cessation of NW growth [27]. Moreover, as the NWs grow longer, the surface area of the NWs increases, which can increase the likelihood of defects and impurities on the NW surface. These defects and impurities can act as etching sites, causing the NWs to break off and reduce their length.

Therefore, the combination of the decrease in precursor concentration and the increased likelihood of defects and impurities can lead to self-termination of the deposited ZnO NWs and decrease their length after 6 h

According to Table 1, surface density and the aspect ratio of the deposited NW followed the same trend. They increased up to 6 h. After that, the surface density, along with the aspect ratio, declined. The sample deposited for 6 h has the highest NW density even if the average diameter of the NW is higher than the NWs deposited for 2 and 4 h. This could be due to

the even distribution and close-packed nature of the NWs deposited.

### Structural characterization

The obtained diffraction patterns are shown in [Fig. 2(a–d)]. All the diffraction patterns agreed with the ZnO hexagonal-phase structure (JCPDS No. 36-1451). The most dominant peaks for the hexagonal ZnO NWs were obtained at the (100), (002), and (101) planes with the  $2\theta$  values of  $31.8^\circ$ ,  $34.43^\circ$ , and  $36.24^\circ$ , respectively. Out of all deposited NWs, (002) is the most dominant peak, which is responsible for the vertical orientation of the NWs.

The degree of preferred orientation of the synthesized NWs was investigated by calculating the texture coefficient  $TC_{hkl}$  using Eq.7 and plotted, as shown in [Fig. 2(e)] [29].

$$TC_{hkl} = \frac{\frac{I_{(hkl)}}{I_{0(hkl)}}}{\frac{1}{N} \sum_N \left( \frac{I_{(hkl)}}{I_{0(hkl)}} \right)} \quad (7)$$

where,  $I_{hkl}$  is the Lorentz curve fitted intensity,  $I_{0(hkl)}$  is the relative intensity of the corresponding plane given in reference data (PDF 00-041-1049), and  $N$  is the number of reflection planes.  $TC_{hkl}$  values represent the enhancement of the  $(hkl)$  reflection compared to a completely randomly oriented sample. According

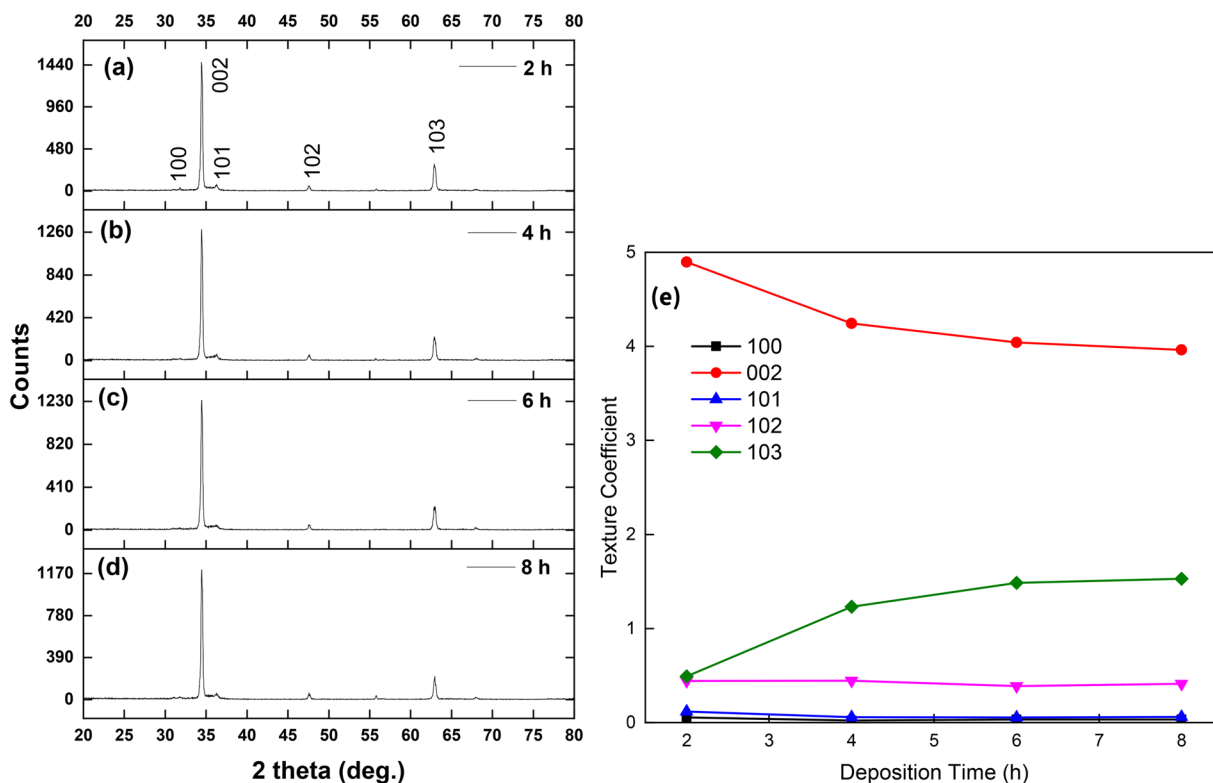


**Figure 2:** GIXRD diffractograms of ZnO Nanowires grown for (a) 2 h (b) 4 h (c) 6 h and (d) 8 h, and (e) corresponding texture coefficient variation of ZnO nanowires.

to [Fig. 2(e)], the deposited NWs were preferentially oriented in the (002) plane.

The Crystallite size of the deposited ZnO NWs was calculated using Debye–Scherrer’s formula [30, 31];

$$D = \frac{0.9\lambda}{\beta \cos\theta} \quad (8)$$

where,  $D$  is crystallite size,  $\lambda$  is the wavelength of the X-ray beam,  $\beta$  is the full width at half maximum (FWHM) of the diffraction peak, and  $\theta$  is the diffraction angle.

Micro strain  $\varepsilon$  measures the lattice imperfection of the ZnO NWs. Micro strain can be calculated using Eq.9 [31, 32];

$$\varepsilon = \frac{\beta \cos\theta}{4} \quad (9)$$

The calculated above values are shown in the Table 2.

The crystallite size of the NWs has slightly increased with the deposition time, which agrees with previous studies [29]. This increment of the crystallite size may be why the Nws deposition for 8 h have larger diameters, as shown in [Fig. 1(g)].

Micro strain is one of the ways which can be used to estimate the imperfections of the lattice. This imperfection can be mainly due to the lattice strains present in the lattice. According to Table 2, lattice imperfection is enhanced by the deposition time due to the increment of the surface area of the NWs with the deposition time described previously.

### Optical characterization

Figure 3 demonstrates the transmittance spectra vs. wavelength between 300–1100 nm. According to the figure, all the obtained spectra showed a bending between the wavelengths of 300–400 nm, which is responsible for the intrinsic band gap of ZnO [7]. Obtained UV transmissions show apparent redshift, which reduces their bandgap from the bandgap of bulk ZnO (3.3 eV).

As a bulk material, ZnO possesses a bandgap of 3.3 eV. Here, the bandgap of deposited ZnO nanowires was calculated using the Tauc method, using Eq. 10 [32];

$$\alpha h\nu = A(h\nu - E_g)^n \quad (10)$$

**TABLE 2:** Calculated structural and optical parameters of deposited ZnO NWs at different deposition times.

Deposition time (h)	Crystallite size (Å)	Microstrain (%)	Band gap (eV)	Urbach energy (eV)
2	408	0.320	3.28	0.267
4	417	0.318	3.22	0.269
6	420	0.312	3.21	0.272
8	430	0.303	3.20	0.273

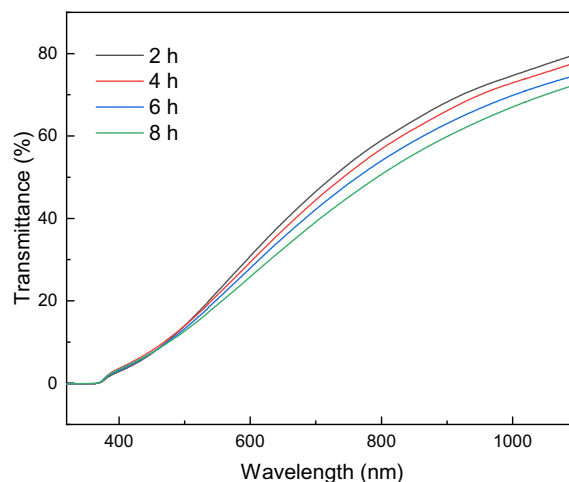


**Figure 3:** The UV–visible spectrum of ZnO nanowires grown at different deposition times.

where  $\alpha$ ,  $h\nu$ ,  $A$ , and  $E_g$  are the absorption coefficient, photon energy, relation constant, and optical bandgap, respectively. ZnO is a direct bandgap semiconductor; hence, the value of  $n$  equals to 2. Band gaps of the seed layers and deposited NWs are calculated by extrapolating the Tauc plots.

Optical absorption edge mainly reduces due to the increment of defect-induced band tailing effect. Urbach energy ( $E_U$ ) describes the band tailing effect. ( $E_U$ ) can be calculated by equation 11 [29]:

$$\alpha = \alpha_0 \exp\left(\frac{E - E_g}{E_U}\right) \quad (11)$$

According to Table 2, the obtained results demonstrate that the increment of deposition time slightly reduces the band gap of the ZnO NWs. During the formation of the ZnO lattice, unsaturated bonds can be formed due to the lack of atoms responsible for the lattice structure. These unsaturated bonds may be the reason for the defects in the lattice, leading to the formation of localized states. With the deposition time, the width of localized states in the optical band gap increases. Thus, the optical absorption edge decreases, reducing the bandgap [29].

### Gas sensing

#### Gas sensing mechanism

Metal oxides can be characterized as either n-type or p-type. The gas sensing mechanism of n-type metal oxides differs from that of p-type metal oxides. Since ZnO belongs to n-type metal oxides, this study focuses on the mechanism of n-type metal oxides. n-type metal oxides are commonly used in chemiresistive gas sensors [33]. Even though the gas-sensing mechanism of metal oxides is not fully understood, oxygen adsorption and

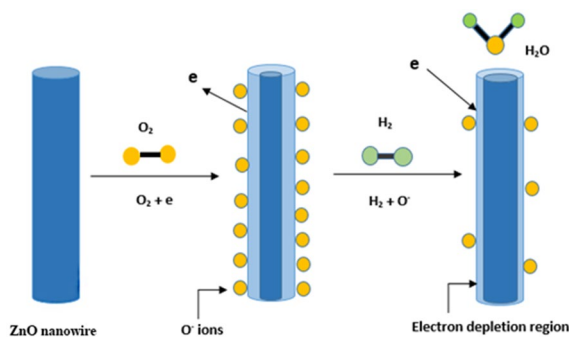
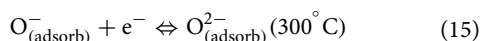
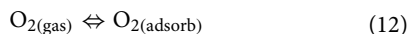
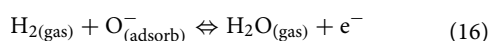


**Figure 4:** Gas sensing mechanism of ZnO nanowires.

desorption theory is considered the most accepted theory to explain this. During the sensing process, the resistance of ZnO NWs changes through the adsorption and desorption of the chemical gases on the surface of ZnO. This is common in all metal oxides. When ZnO is exposed to air, the oxygen molecules are adsorbed to the surface of ZnO by forming  $O^-$ ,  $O_2^-$ ,  $O_2^-$  ions by capturing electrons from the conduction band of the metal oxide. This leads to the formation of an electron depletion region underneath the ZnO surface. Out of these,  $O^-$  is the most reactive species, forming between 100–300 °C. The electron deficiency of the conduction band will enhance the resistance of the metal oxide [33–35] as shown in Fig. 4.



There are two types of gases in the environment: reducing gases and oxidizing gases. The reaction mechanism of reducing gases converses with the sensing mechanism of oxidizing gases.  $H_2$  is a reducing gas. As shown in Fig. 4, when the sensor is exposed to  $H_2$ , the adsorbed oxygen ions on the surface of the metal oxide will react with  $H_2$  molecules to form  $H_2O$  and release it into the atmosphere. This is a chemisorption process. During the reaction, oxygen ions release electrons back into the conduction band, reducing the thickness of the electron depletion region. Therefore, the electron density of the conduction band increases by decreasing the resistance of the metal oxide.



The response of a gas sensor refers to the change in its electrical signal, typically a voltage or current, that occurs when it

detects the gas. The response of a gas sensor is crucial since it determines the sensor’s sensitivity and precision in identifying the target gas. A sensor with a high response can detect gases at low concentrations, whereas a sensor with a poor response could need to detect gases at higher concentrations. For quick and accurate detection, it is critical to consider a gas sensor’s response time or the amount of time it takes for the sensor to notice a change in the gas concentration. The response of the sensor is calculated by Eq. 17 [36, 37];

$$\text{Response (S)} = \frac{R_a}{R_g} \quad (17)$$

where  $R_a$  is the electrical resistance of the sensor in the presence of the  $O_2$  gas ambient, and  $R_g$  is the resistance of the sensor while the sensor exposed to the target gas ambient.

1 D nanostructured sensing materials are highly sensitive compared to other nanostructures as they provide more reaction sites for the gases. Also, it can provide high surface energy [33], which will enhance the gas sensing performance. Grain size and crystallinity are two of the other factors affecting gas sensing performance. Also, the wire-to-wire junction, along with the inter-wire junction regions present in closely packed, well-oriented NWs, act as an additional conduction pathway for charge carriers in the sensor, which enhances the sensitivity of a gas sensor [33].

### Gas sensing results

Deposited ZnO NWs were used to fabricate gas sensing devices and characterized by measuring the response towards  $H_2$  gas. The change in resistance of the sensors was calculated by measuring the change in current at a fixed voltage in the presence of the  $H_2$  gas.

First, all four sensors were exposed to 100 ppm  $H_2$  in the air at various operating temperatures. The temperature was varied from 50–200 °C in 50 °C temperature increments for all four sensors. According to the results obtained, the responses of the sensors fluctuated with the temperature, as shown in [Fig. 5(a)]. With the temperature, the response increased and reached its peak position before decreasing with further temperature increments. Overall, the highest response was obtained at 100 °C.

During the chemisorption model,  $O_2$  molecules adsorb to the surface of n-type metal oxides to form superoxides. Below 100 °C, the  $O_2$  molecules are reduced to form  $O_2^-$  ions, while it forms  $O^-$  ions between 100–300 °C and  $O^{2-}$  ions above 300 °C. Within these types,  $O^-$  is the most reactive superoxide species. At 100 °C,  $O_2$  forms more  $O^-$  ions on the surface than at other temperatures. Hence, the increase of the resistance in ZnO is higher than in others. When exposed to  $H_2$ , a high concentration of  $O^-$  ions react with  $H_2$  to form  $H_2O$ . Due to that, the resistance of the ZnO dramatically changes. The concentration

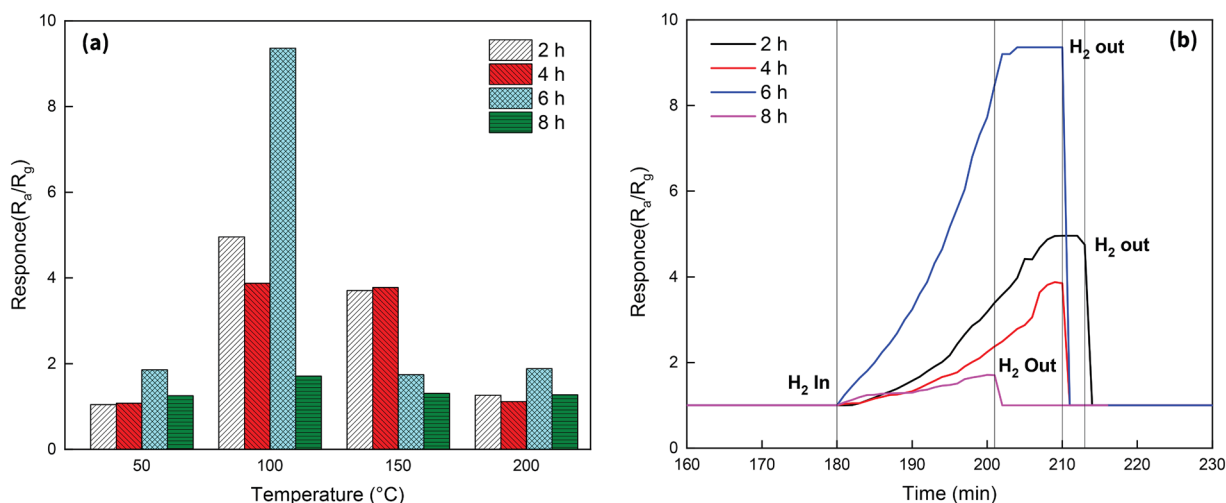


**Figure 5:** (a) Response variation of the four different sensors at different operating temperatures and (b) Response variation of the sensors deposited on different deposition times towards 100 ppm H<sub>2</sub> at the optimum temperature of 100 °C.

of O<sup>-</sup> produced below and above 100 °C is comparatively low, and between these two ends, O<sub>2</sub> tend to form O<sub>2</sub><sup>-</sup> and O<sup>2-</sup> ions, respectively. Therefore, the resistance change decreases during these temperatures [34, 35].

Another reason for this observation is that energy generated during the reducing reaction is not enough at low temperatures to overcome the energy barrier. Hence, the responses can be low at 50 °C [34]. Further, at higher temperatures, depletion length decreases because the rate of adsorption is overcome by the rate of desorption. As a result, the gas response decreases at higher temperatures [34].

Figure 5(b) illustrates the change in response of the sensors at 100 ppm H<sub>2</sub> gas at the optimum temperature of 100 °C. According to that, the sensor with the 6 h deposition duration yielded the highest response of 9.36 at 100 °C. The surface-to-volume ratio of the structure plays a crucial role in gas sensors. The higher surface-to-volume ratio will lead to higher sensitivity in sensors. According to Table 1, NWs deposited for 2 h has the highest surface-to-volume ratio. Even though the NWs deposited for 2 h have the highest surface-to-volume ratio, the NWs grown for 6 h are responsible for the highest surface density and the lowest crystallinity over the others. Surface density also positively affects the response because higher surface density means the number of NWs is higher, creating more reactive sites. This will increase the adsorption and desorption process while increasing the sensor's response. ZnO NWs with higher crystallinity exhibit better gas-sensing performance than those with lower crystallinity [33, 38]. Highly crystalline ZnO NWs have a more ordered and well-defined surface structure, which provides more active sites for gas molecules to bind and interact with. This increases the sensitivity of the NWs to gas molecules

and thus results in a higher gas-sensing response. When comparing all these factors, the sensor in which NWs are grown for 6 h has the highest probability of obtaining a better response over the sensor with 2 h deposition time.

## Conclusion

The chemical bath deposition technique was effectively used to deposit hexagonal ZnO NWs on borosilicate substrates. As the deposition duration was increased, the diameter, length, and aspect ratio of the deposited NW were found to increase up to 6 h, before decreasing at 8 h. NWs deposited for 2 h had the lowest diameter, while the ones deposited for 8 h had the highest. The highest length, surface density and aspect ratio were obtained by the NWs grown for 6 h, while the NWs deposited for 8 h had the lowest. The ZnO gas sensors were later fabricated using the grown ZnO NWs. The gas sensing ability of the ZnO NWs was investigated based on their response to H<sub>2</sub> gas at different operating temperatures. The sensors showed an optimum response of 9.36 for 100 ppm H<sub>2</sub> gas at 100 °C for the ZnO NWs grown for 6 h.

## Materials and methods

### Substrate cleaning

First, borosilicate substrates were cut into 2.5 cm × 2.0 cm pieces. Then, substrates were cleaned according to the standard chemical cleaning procedure [29, 39] before being stored in a desiccator. The substrates were then plasma cleaned for 5 min to obtain a better hydrophilic surface.

### Preparation of ZnO seed layers

ZnO seed solution was prepared by mixing 0.1 M solutions of Zinc acetate dehydrate [ $\text{Zn}(\text{CH}_3\text{COO})_2 \cdot 2\text{H}_2\text{O}$ —99.5%] and monoethanolamine (MEA) [ $\text{NH}_2\text{CH}_2\text{CH}_2\text{OH}$ ] in equimolar ratio (1). The solution was sonicated for 15 min and stirred for 2 h at 300 rpm and 70 °C. The resulting milky solution was aged for 24 h at room temperature. The solution was then spray-coated on the cleaned glass substrate. Then, the substrates were annealed in air at 300 °C for an hour.

### Preparation of ZnO NWs

ZnO NWs were grown with an equimolar (0.1 M) aqueous solution of zinc nitrate hexahydrate [ $\text{Zn}(\text{NO}_3)_2 \cdot 6\text{H}_2\text{O}$  – 99.5%] and HMTA [ $\text{C}_6\text{H}_{12}\text{N}_4$  – 99.5%]. The prepared substrates with seed layers were used for CBD at 90 °C at a stirring rate of 700 rpm. The deposition duration was varied as 2, 4, 6, and 8 h. After that, samples were rinsed with DI water and dried in air. Finally, the samples were annealed in air at 300 °C for half an hour.

### Characterization techniques

The morphology of the NWs was studied using the Zeiss EVO LS 15 field emission scanning electron microscope (FE-SEM). Structural characteristics were investigated using grazing incident X-ray diffractograms (GIXRD) obtained from Bruker D8 Advance with Cu  $K\alpha$  ( $\lambda = 1.5406 \text{ \AA}$ ) X-ray photons incident at an angle of 1° and 0.02° intervals from 20° up to 80°. The optical analysis was conducted using a Shimadzu UV-1800 double-beam spectrophotometer.

The  $\text{H}_2$  gas sensor was devised using the synthesized ZnO NWs using Cu electrodes. The sensor was placed on a substrate heater inside a gas flow chamber, where the temperature was controlled using a PLD temperature controller. A constant voltage was maintained between the electrodes, and the current was measured using a picometer. The resistance changes of the sensor were measured at 50, 100, 150, and 200 °C at a concentration of 100 ppm of  $\text{H}_2$ . A schematic of the gas sensor fabricated is shown in Fig. 6.

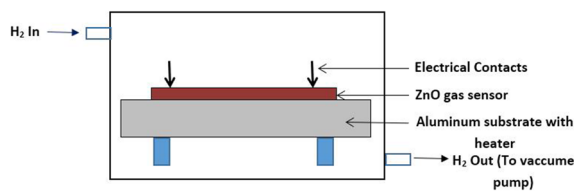


**Figure 6:** Schematic of the gas sensing device fabricated.

### Acknowledgments

Financial assistance from the Responsive Research Seed Grant of Sri Lanka Technological Campus, Padukka, Sri Lanka (Grant No RRSg/20/A2) is acknowledged. Postgraduate Institute of Science, University of Peradeniya, Sri Lanka, Department of Physics, University of Peradeniya, Sri Lanka, are acknowledged for instrumental as well as technical support provided.

### Author contributions

YKA: conceptuzation, data curation, methodology, investigation, formal analysis, writing—original draft. AAIL: methodology, investigation, formal analysis. MAHMM: conceptuzation, investigation, supervision, writing—review & editing, project administration. BSD: conceptuzation, investigation, supervision, writing—review & editing. NG: conceptuzation, investigation, supervision, writing—review & editing, project administration.

### Data availability

The datasets generated during and/or analyzed during the current study are available from the corresponding author on reasonable request

### Declarations

**Conflict of interest** The authors declare that they have no conflict of interest.

### References

1. N. Konno, S. Mizuno, H. Nakaji, Y. Ishikawa, Development of compact and high-performance fuel cell stack. *SAE Int. J. Altern. Powertrains* **4**(1), 123–129 (2015). <https://doi.org/10.4271/2015-01-1175>
2. D.T. Koch, E. Eßer, S. Kureti, A. Sousa,  $\text{H}_2$ -denox catalyst for  $\text{H}_2$  combustion engines. *MTZ worldw.* **81**(6), 30–35 (2020). <https://doi.org/10.1007/s38313-020-0229-3>
3. T. Hübert, L. Boon-Brett, G. Black, U. Banach, Hydrogen sensors - a review. *Sens. Actuators B: Chem.* **157**(2), 329–352 (2011). <https://doi.org/10.1016/j.snb.2011.04.070>
4. T.V. Khai, L.V. Thu, L.T.T. Ha, V.M. Thanh, T.D. Lam, Structural, optical and gas sensing properties of vertically well-aligned ZnO nanowires grown on graphene/Si substrate by thermal evaporation method. *Mater. Charact.* **141**, 296–317 (2018). <https://doi.org/10.1016/j.matchar.2018.04.047>
5. G.Z. Xing, J.B. Yi, J.G. Tao, T. Liu, L.M. Wong, Z. Zhang, G.P. Li, S.J. Wang, J. Ding, T.C. Sum, C.H.A. Huan, T. Wu, Comparative study of room-temperature ferromagnetism in Cu-doped ZnO nanowires enhanced by structural inhomogeneity.



- Adv. Mater. **20**(18), 3521–3527 (2008). <https://doi.org/10.1002/adma.200703149>
6. S.R. Bhattacharyya, Z. Mallick, R.N. Gayen, Vertically aligned Al-doped ZnO nanowire arrays as efficient photoanode for dye-sensitized solar cells. *J. Electron. Mater.* **49**(6), 3860–3868 (2020). <https://doi.org/10.1007/s11664-020-08107-9>
  7. Y. Li, X. Zhao, W. Fan, Structural, electronic, and optical properties of Ag-doped ZnO nanowires: first principles study. *J. Phys. Chem. C* **115**(9), 3552–3557 (2011). <https://doi.org/10.1021/jp1098816>
  8. K.M. McPeak, J.B. Baxter, ZnO nanowires grown by chemical bath deposition in a continuous flow microreactor. *Cryst. Growth Des.* **9**(10), 4538–4545 (2009). <https://doi.org/10.1021/cg900551f>
  9. A. Kaphle, M.F. Borunda, P. Hari, Influence of cobalt doping on residual stress in ZnO nanorods. *Mater. Sci. Semicon. Process.* **84**, 131–137 (2018). <https://doi.org/10.1016/j.mssp.2018.05.019>
  10. N. Tit, W. Othman, A. Shaheen, M. Ali, High selectivity of n-doped ZnO nano-ribbons in detecting H<sub>2</sub>, O<sub>2</sub> and CO<sub>2</sub> molecules: effect of negative-differential resistance on gas-sensing. *Sens. Actuators B: Chem.* **270**, 167–178 (2018). <https://doi.org/10.1016/j.snb.2018.04.175>
  11. A.Z. Sadek, W. Wlodarski, K. Kalantar-zadeh, S. Choopun, ZnO nanobelt based conductometric H<sub>2</sub> and NO<sub>2</sub> gas sensors. *IEEE* (2005). <https://doi.org/10.1109/icsens.2005.1597952>
  12. Z. Fu-Chun, Z. Zhi-Yong, Z. Wei-Hu, Y. Jun-Feng, Y. Jiang-Ni, First-principles study of the electronic and optical properties of ZnO nanowires. *Chin. Phys. B* **18**(6), 2508–2513 (2009). <https://doi.org/10.1088/1674-1056/18/6/065>
  13. Y.R. Ryu, S. Zhu, J.D. Budai, H.R. Chandrasekhar, P.F. Miceli, H.W. White, Optical and structural properties of ZnO films deposited on GaAs by pulsed laser deposition. *J. Appl. Phys.* **88**(1), 201–204 (2000). <https://doi.org/10.1063/1.373643>
  14. X. Liu, X. Wu, H. Cao, R.P.H. Chang, Growth mechanism and properties of ZnO nanorods synthesized by plasma-enhanced chemical vapor deposition. *J. Appl. Phys.* **95**(6), 3141–3147 (2004). <https://doi.org/10.1063/1.1646440>
  15. K.R. Nandanapalli, D. Mudusu, Surface passivated zinc oxide (ZnO) nanorods by atomic layer deposition of ultrathin ZnO layers for energy device applications. *ACS Appl. Nano.* **1**(8), 4083–4091 (2018). <https://doi.org/10.1021/acsanm.8b00816>
  16. C.H. Bae, S.M. Park, S.-E. Ahn, D.-J. Oh, G.T. Kim, J.S. Ha, Sol-gel synthesis of sub-50 nm ZnO nanowires on pulse laser deposited ZnO thin films. *Appl. Surf. Sci.* **253**(4), 1758–1761 (2006). <https://doi.org/10.1016/j.apsusc.2006.03.006>
  17. C. Min, X. Shen, W. Sheng, Microwave-assisted aqueous synthesis of ultralong ZnO nanowires: photoluminescence and photovoltaic performance for dye-sensitized solar cell. *Appl. Phys. A* **96**(4), 799–803 (2009). <https://doi.org/10.1007/s00339-009-5299-7>
  18. H. Hu, X. Huang, C. Deng, X. Chen, Y. Qian, Hydrothermal synthesis of ZnO nanowires and nanobelts on a large scale. *Mater. Chem. Phys.* **106**(1), 58–62 (2007). <https://doi.org/10.1016/j.matchemphys.2007.05.016>
  19. C. Lausecker, B. Salem, X. Baillin, V. Consonni, Implementing the reactor geometry in the modeling of chemical bath deposition of ZnO nanowires. *Nanomaterials* **12**(7), 1069 (2022). <https://doi.org/10.3390/nano12071069>
  20. F.D. Nayeri, E.A. Soleimani, F. Salehi, Synthesis and characterization of ZnO nanowires grown on different seed layers: the application for dye-sensitized solar cells. *Renew. Energy* **60**, 246–255 (2013). <https://doi.org/10.1016/j.renene.2013.05.006>
  21. Y. Tak, K. Yong, Controlled growth of well-aligned ZnO nanorod array using a novel solution method. *J. Phys. Chem. B* **109**(41), 19263–19269 (2005). <https://doi.org/10.1021/jp0538767>
  22. R. Devaraj, K. Venkatachalam, P.M. Razad, Role of seed layer: lattice orientation attachment and structural stabilization on the lateral growth of ZnO nanorods. *J. Mater. Sci.: Mater. Electron.* **27**(4), 4011–4018 (2016). <https://doi.org/10.1007/s10854-015-4255-x>
  23. L.-W. Ji, S.-M. Peng, J.-S. Wu, W.-S. Shih, C.-Z. Wu, I.-T. Tang, Effect of seed layer on the growth of well-aligned ZnO nanowires. *J. Phys. Chem. Solids* **70**(10), 1359–1362 (2009). <https://doi.org/10.1016/j.jpcs.2009.07.029>
  24. S.-F. Wang, T.-Y. Tseng, Y.-R. Wang, C.-Y. Wang, H.-C. Lu, W.-L. Shih, Effects of preparation conditions on the growth of ZnO nanorod arrays using aqueous solution method. *Int. J. Appl. Ceram. Technol.* **5**(5), 419–429 (2008). <https://doi.org/10.1111/j.1744-7402.2008.02242.x>
  25. R. Parize, J. Garnier, O. Chaix-Pluchery, C. Verrier, E. Appert, V. Consonni, Effects of hexamethylenetetramine on the nucleation and radial growth of ZnO nanowires by chemical bath deposition. *J. Phys. Chem. C* **120**(9), 5242–5250 (2016). <https://doi.org/10.1021/acs.jpcc.6b00479>
  26. M. Poornajar, P. Marashi, D.H. Fatmehsari, M.K. Esfahani, Synthesis of ZnO nanorods via chemical bath deposition method: the effects of physicochemical factors. *Ceram. Int.* **42**(1), 173–184 (2016). <https://doi.org/10.1016/j.ceramint.2015.08.073>
  27. A.H. Rakhsha, H. Abdizadeh, E. Pourshaban, M.R. Golobostanfard, V.R. Mastelaro, M. Montazerian, Ag and Cu doped ZnO nanowires: a pH-controlled synthesis via chemical bath deposition. *Materialia* **5**, 100212 (2019). <https://doi.org/10.1016/j.mtla.2019.100212>
  28. Y.-C. Huang, J. Zhou, K. Nomenyo, R.E. Ionescu, A. Gokarna, G. Lerondel, Facile, wafer-scale compatible growth of ZnO nanowires via chemical bath deposition: assessment of zinc ion contribution and other limiting factors. *Nanoscale Adv.* **2**(11), 5288–5295 (2020). <https://doi.org/10.1039/d0na00434k>
  29. A.A.I. Lakmal, R.K.K.G.R.G. Kumarasinghe, V.A. Seneviratne, J.-Y. Chen, J.-M. Song, B.S. Dassanayake, Thermally evaporated CdS thin films for CdS/CdTe solar cells: effect of substrate

- temperature on CdS layer. *Mater. Sci. Eng.* **273**, 115406 (2021). <https://doi.org/10.1016/j.mseb.2021.115406>
30. J. Sultana, S. Paul, R. Saha, S. Sikdar, A. Karmakar, S. Chattopadhyay, Optical and electronic properties of chemical bath deposited p-CuO and n-ZnO nanowires on silicon substrates: p-CuO/n-ZnO nanowires solar cells with high open-circuit voltage and short-circuit current. *Thin Solid Films* **699**, 137861 (2020). <https://doi.org/10.1016/j.tsf.2020.137861>
  31. S. Senthilarasu, Thermally evaporated ZnPc thin films-band gap dependence on thickness. *Sol. Energy Mater. Sol. Cells* **82**(1–2), 179–186 (2004). <https://doi.org/10.1016/j.solmat.2004.01.016>
  32. M.B. Rabeh, N. Khedmi, M.A. Fodha, M. Kanzari, The effect of thickness on optical band gap and N-type conductivity of CuInS<sub>2</sub> thin films annealed in air atmosphere. *Energy Procedia* **44**, 52–60 (2014). <https://doi.org/10.1016/j.egypro.2013.12.009>
  33. B. Yang, N.V. Myung, T. Tran, 1d metal oxide semiconductor materials for chemiresistive gas sensors: a review. *Adv. Electron. Mater.* **7**(9), 2100271 (2021). <https://doi.org/10.1002/aelm.202100271>
  34. B. Mondal, B. Basumatari, J. Das, C. Roychaudhury, H. Saha, N. Mukherjee, ZnO–SnO<sub>2</sub> based composite type gas sensor for selective hydrogen sensing. *Sens. Actuators B: Chem.* **194**, 389–396 (2014). <https://doi.org/10.1016/j.snb.2013.12.093>
  35. S. Choopun, N. Hongsith, E. Wongrat, Metal-Oxide Nanowires for Gas Sensors. *InTech* (2012). <https://doi.org/10.5772/54385>
  36. Q. Wan, Q.H. Li, Y.J. Chen, T.H. Wang, X.L. He, J.P. Li, C.L. Lin, Fabrication and ethanol sensing characteristics of ZnO nanowire gas sensors. *Appl. Phys. Lett.* **84**(18), 3654–3656 (2004). <https://doi.org/10.1063/1.1738932>
  37. Y. Wang, X. Wu, Y. Li, Z. Zhou, Mesostructured SnO<sub>2</sub> as sensing material for gas sensors. *Solid-State Electronics* **48**(5), 627–632 (2004). <https://doi.org/10.1016/j.sse.2003.09.015>
  38. A. Ramadhan, N.L.W. Septiani, W.A.E. Prabowo, A. Melati, Temperature effect of chemical bath deposition (CBD) to fabrication and characterization of zinc oxide nanorods thin films based gas sensing: ethanol. *J. Phys.: Conf. Ser.* **1445**(1), 012017 (2020). <https://doi.org/10.1088/1742-6596/1445/1/012017>
  39. W.G.C. Kumarage, R.P. Wijesundera, V.A. Seneviratne, C.P. Jayalath, B.S. Dassanayake, Tunable optoelectronic properties of CBD-CdS thin films via bath temperature alterations. *J. Phys. D: Appl. Phys.* **49**(9), 095109 (2016). <https://doi.org/10.1088/0022-3727/49/9/095109>

**Publisher's Note** Springer Nature remains neutral with regard to jurisdictional claims in published maps and institutional affiliations.

Springer Nature or its licensor (e.g. a society or other partner) holds exclusive rights to this article under a publishing agreement with the author(s) or other rightsholder(s); author self-archiving of the accepted manuscript version of this article is solely governed by the terms of such publishing agreement and applicable law.